quire an additional contact point whereas ends lose one when chains are broken. Accounting for the contribution of the cohesive energy, δ (in units of u_d) the defect energies shift like $\varepsilon_3 \rightarrow \varepsilon_3 - 1/2\delta$ and $\varepsilon_1 \rightarrow \varepsilon_1 + 1/2\delta$. In particular, the critical temperature increases like $T_c^* \rightarrow T_c^* + 1.05\delta$ and the reentrant coexistence curve evolves to a parabolic shape, typical of isotropic fluids (Fig. 3B). The crucial influence that the shape of the particles, their short-range interaction, and polydispersity have on their phase behavior can therefore be tested by measurement of the shape of the coexistence curve.

References and Notes

1. R. E. Rosensweig, *Science* **271**, 614 (1996).
2. T. C. Halsey, *Science* **258**, 761 (1992).
3. Of course, if enough isotropic attraction is added (e.g., van der Waals dispersion interaction), the usual isotropic three-dimensional aggregation is restored, and the resulting LGT does occur. However, the interesting and controversial point is whether phase separation can be driven by the dipolar interaction alone.
4. M. E. van Leeuwan, B. Smit, *Phys. Rev. Lett.* **71**, 3991 (1993).
5. M. J. Stevens, G. S. Grest, *Phys. Rev. Lett.* **72**, 3686 (1994).
6. D. Levesque, J. J. Weis, *Phys. Rev. E* **49**, 5131 (1994).
7. J. M. Tavares, J. J. Weis, M. M. Telo da Gama, *Phys. Rev. E* **59**, 4388 (1999).
8. P. G. de Gennes, P. A. Pincus, *Phys. Kondens. Mater.* **11**, 189 (1970).
9. A. P. Gast, C. F. Zukoski, *Adv. Colloid Interface Sci.* **30**, 153 (1989) .
10. R. P. Sear, *Phys. Rev. Lett.* **76**, 2310 (1996).
11. R. van Roij, *Phys. Rev. Lett.* **76**, 3348 (1996).
12. Y. Levin, *Phys. Rev. Lett.* **83**, 1159 (1999).
13. P. J. Camp, J. C. Shelley, G. N. Patey, *Phys. Rev. Lett.* **84**, 115 (2000).
14. E. Dubois, V. Cabuil, F. Boué, R. Perzynski, *J. Chem. Phys.* **111**, 7147 (1999).
15. In their system, the particles are relatively small and the resulting dipolar interactions are weak. The formation of long chains is thus not likely, and our model of defect-induced phase separation may not apply.
16. S. Banerjee, R. B. Griffiths, M. Widom, *J. Stat. Phys.* **93**, 109 (1998).
17. This may be demonstrated by considering one spherical particle that belongs to an infinite, straight chain. The interaction of one sphere with the rest of the chain is
$$-2u_d \sum_{n=1}^{\infty} n^{-3} = -2u_d\zeta(3)$$
which is only $\zeta(3) - 1 \simeq 20\%$ larger than the interaction of the sphere with its two nearest neighbors, $-2u_d$.
18. Although junctions of even higher coordination number are also possible, they occur very rarely due to their higher energetic cost and lower entropy.
19. J. C. Wheeler, P. Pfeuty, *J. Chem. Phys.* **74**, 6415 (1981).
20. T. J. Drye, M. E. Cates, *J. Chem. Phys.* **96**, 1367 (1992).
21. T. Tlusty, R. Menes, S. A. Safran, R. Strey, *Phys. Rev. Lett.* **78**, 2616 (1997).
22. A. Bernheim-Grosswasser, T. Tlusty, S. A. Safran, Y. Talmon, *Langmuir* **15**, 5448 (1999).
23. P. G. de Gennes, *Scaling Concepts in Polymer Physics* (Cornell Univ. Press, Ithaca, NY, 1979), chaps. IX–X.
24. Minimizing the ideal-gas free energy of noninteracting defects, $f_d = k_B T\rho_d (\ln\rho_d - 1) + \rho_d\varepsilon_d$, where ρ_d is the density of the defects and ε_d their energy cost, one finds the optimal density $\rho_d^* = e^{-\varepsilon_d}/k_B T$ and the minimal free energy, $f_d^* = -k_B T\rho_d^*$.
25. Thinking of the self-assembling chains as the edges of a graph whose vertices are either junctions or ends, one finds that the density of vertices is $v = \rho_1 + \rho_3$ whereas the density of edges is $e = 1/2\rho_1 + 3/2\rho_3 = v + 1/2(\rho_1 - \rho_3)$. This implies that at the critical point $e = v = 2\rho_1 = 2\rho_3$, the minimal graph connecting v vertices, a tree with $e = v$ edges, becomes thermodynamically feasible.
26. T. Tlusty, S. A. Safran, R. Strey, *Phys. Rev. Lett.* **84**, 1244 (2000).
27. K. Sano, M. Doi, *J. Phys. Soc. Jpn.* **52**, 2810 (1983).
28. J. C. Shelley, G. N. Patey, D. Levesque, J. J. Weis, *Phys. Rev. E* **59**, 3065 (1999).
29. S. C. McGrother, G. Jackson, *Phys. Rev. Lett.* **76**, 4183 (1996).
30. We acknowledge fruitful discussions with J. Klein, R. E. Rosensweig, P. A. Pincus, and A. Zilman and support from The Israel Science Foundation center on Self-Assembly and the donors of the Petroleum Research Fund, administrated by the American Chemical Society.

9 August 2000; accepted 22 September 2000

Macroscopic Fibers and Ribbons of Oriented Carbon Nanotubes

**Brigitte Vigolo,[1] Alain Pénicaud,[1] Claude Coulon,[1]
Cédric Sauder,[2] René Pailler,[2] Catherine Journet,[3]*
Patrick Bernier,[3] Philippe Poulin[1]†**

A simple method was used to assemble single-walled carbon nanotubes into indefinitely long ribbons and fibers. The processing consists of dispersing the nanotubes in surfactant solutions, recondensing the nanotubes in the flow of a polymer solution to form a nanotube mesh, and then collating this mesh to a nanotube fiber. Flow-induced alignment may lead to a preferential orientation of the nanotubes in the mesh that has the form of a ribbon. Unlike classical carbon fibers, the nanotube fibers can be strongly bent without breaking. Their obtained elastic modulus is 10 times higher than the modulus of high-quality bucky paper.

Theoretical predictions (*1*, *2*) and measurements on individual objects (*3*–*5*) suggest that single-walled carbon nanotubes (SWNTs) (*6*) could form the basis of materials with exceptional mechanical and electromechanical properties. Despite their intrinsic rigidity and high anisotropy, the currently available macroscopic forms of SWNTs are isotropic and rather fragile. These forms mainly consist of raw powder-like materials originating from synthesis (*7*, *8*), suspensions in solvents (*9*), and thin mats, known as bucky paper, obtained by drying SWNT suspensions (*10*). Processing nanotubes on macroscopic scales to obtain materials with more practical uses is a major challenge. Here we report a simple and versatile approach that can create rigid fibers and ribbons of preferentially oriented SWNTs (*11*). Our processing consists of dispersing the nanotubes in surfactant solutions and then recondensing the nanotubes in the stream of a polymer solution. In contrast to most ordinary carbon fibers, SWNT fibers can be strongly bent and even tightly tied without breaking. Although they are still weak under tension, these recently obtained SWNT fibers are already 10 times stronger than high-quality bucky paper, the main macroscopic form of SWNT nanotubes used so far (*12*).

The raw material we used was produced with the electric-arc technique (*8*). This technique produces SWNTs in the form of bundles of a few nanotubes, along with a certain fraction of carbon impurities and catalysts. This material was sonicated in aqueous solutions of sodium dodecyl sulfate (SDS), a surfactant that adsorbs at the surface of the nanotube bundles. At low surfactant concentrations, large and dense clusters of the initial material were still found after sonication. The amount of surfactant was too low to produce an efficient coating and induce electrostatic repulsions that could counterbalance van der Waals attractions (*13*). At higher SDS concentrations, black and apparently homogeneous suspensions were obtained. These suspensions did not coarsen or phase-separate macroscopically over several weeks. However, as revealed by optical microscopy (Fig. 1), dielectric measurements, and electron microscopy of freeze-fractured samples, these systems can in fact exhibit distinct phases. At intermediate concentrations of SDS, SWNTs were homogeneously dispersed and formed a single phase. The viscosity of these systems was almost that of pure water. In this regime, the electrostatic repulsion provided by adsorbed surfactants stabilized the nanotubes against van der Waals attraction. However, at higher SDS concentrations, a texture that reflected the formation of light clusters was observed. The clusters, which did not coarsen over several weeks,

---

[1] Centre de Recherche Paul Pascal/CNRS, Université Bordeaux I, Avenue Schweitzer, 33600 Pessac, France. [2] Laboratoire des Composites Thermostructuraux, Allée de la Boëtie, 33600 Pessac, France. [3] Groupe de Dynamique des Phases Condensées, Université de Montpellier II, 34095 Montpellier, France.

*Present address: Université Claude Bernard, Lyon I, 43 boulevard du 11 novembre 1918, 69622 Villeurbanne, France.

†To whom correspondence should be addressed. E-mail: poulin@crpp.u-bordeaux.fr

coexisted with dispersed nanotubes, which suggests that attractive interactions take place when the surfactant concentration is increased. The clusters became larger and denser with increasing surfactant concentration, and the viscosity of the suspensions increased significantly. Such a behavior can presumably be ascribed to the increasing concentration of surfactant aggregates, known as micelles (*13*), in the aqueous solution. Micelles cannot fit in between two bundles that are close to each other. As a result, the osmotic pressure of the micelles around bundles creates an effective attraction. In classical colloidal suspensions (*14*) and in multiwall nanotube dispersions (*15*), this attraction is known as a depletion attraction.

Van der Waals–induced aggregation at low SDS concentration and depletion-induced aggregation at high SDS concentration delimit an intermediate domain of homogeneously dispersed nanotubes. This domain of the phase diagram exhibits an optimum at about 0.35 weight % (wt%) in nanotubes and 1.0 wt% in SDS. Subsequent processing steps were optimized at that composition because it corresponds to the maximum amount of SWNTs for which we could obtain homogeneous dispersions.

These solutions are reminiscent of homogeneous solutions of rigid polymers (*16*) or anisotropic colloids (*17*). They are thus potentially useful for orienting carbon nanotubes in the field of a laminar flow. In order to make permanent structures, our processing was designed so that the nanotube bundles stuck to each other while they were oriented in a preferential direction by a given flow. Nanotube aggregation was obtained by injecting the SWNT dispersion in the co-flowing stream of a polymer solution that contained 5 wt% of polyvinylalcohol (PVA) (molecular weight, 70000; hydrolysis, 89%; solution viscosity, ~200 cP). The addition of PVA to suspensions initially stabilized by SDS induced aggregation of the nanotubes at rest, as in flowing systems. Because of its amphiphilic character, the PVA presumably adsorbs onto the tubes and displaces some SDS molecules. In contrast to SDS, PVA does not provide an efficient stabilization against van der Waals attractions. As shown schematically in Fig. 2, the SWNT dispersion was slowly injected through a syringe needle (0.5 mm in diameter) or a thin glass capillary (with a rectangular section of 0.5 mm by 50 μm or 1 mm by 100 μm). Under these conditions, as for solutions of rigid polymers or anisotropic colloids (*16*, *17*), flow-induced alignment of the nanotubes is expected in the direction of the fluid velocity. Because the polymer solution is more viscous than the nanotube dispersion, we may expect a shear contribution in the flow at the tip of the capillary; that is, gradients of the velocity field perpendicular to the fluid velocity. The flow-induced alignment may somehow be maintained by the PVA solution, because it allows the nanotubes to be rapidly stuck together as they are coming out of the capillary tube. This process leads to the formation of long ribbons that remain stable in the absence of flow. Their cross section is on the order of the cross section of the capillary tube or the diameter of the syringe needle. However, the exact dimensions of the cross section depend on the injection rate and flow conditions. Qualitatively, the ribbons become thicker and larger when the speed of the co-flowing polymer solution is lowered and the injection rate is increased. This behavior strongly suggests that, in addition to the shear flow, there is also an important contribution from elongational flow; that is, velocity gradients along the fluid velocity. When drawn in two dimensions, the ribbon forms a spiral. It is thus difficult to make long ribbons without entanglements after several turns. By pumping the polymer solution from the bottom, meter-long ribbons can be easily drawn. Indeed, under these conditions the ribbons grow in the form of a three-dimensional helical structure.

We used optical microscopy between crossed polarizers to examine the anisotropy of the ribbons. The transmitted light intensity depended on the relative orientation of the ribbon with respect to the optical axis of the polarizers (Fig. 3A). This observation confirms that the nanotubes have been aligned in the flow and that a preferential orientation is maintained as the nanotubes stick to each other. The ribbons can be washed and rinsed several times with pure water so that PVA and SDS desorb. They can also be dried when deposited onto flat substrates. A weaker optical anisotropy was still observed in clean and dry ribbons. In spite of structural modifications arising from the drying, scanning electron microscopy of dried ribbons revealed a preferential orientation of the nanotubes along the ribbon's main axis. A typical picture is shown in Fig. 4A. Nanotube bundles and a significant amount of spherical impurities were observed. These common impurities come from the synthesis process and are mostly composed of carbon (*8*). In spite of their presence, we observed that the

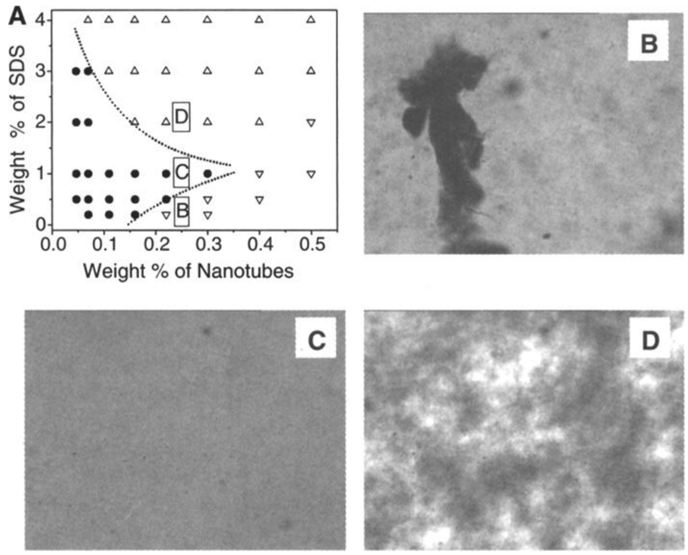

Fig. 1. (**A**) Phase diagram of the SDS/SWNT/water system. At low concentrations of SDS (▽), large dense clusters of the initial material are still found after sonication. At intermediate concentrations of SDS (●), homogeneous dispersions are obtained. This domain exhibits an optimum for about 0.35 wt% of SWNTs and 1.0 wt% of SDS. As observed with optical microscopy, light clusters of aggregated SWNTs form a texture at high concentrations of SDS (△). (**B** to **D**) A series of optical micrographs taken for the same SWNT concentrations and different amounts of SDS indicated at points B, C, and D in (A). The horizontal dimension of each picture is 300 μm.

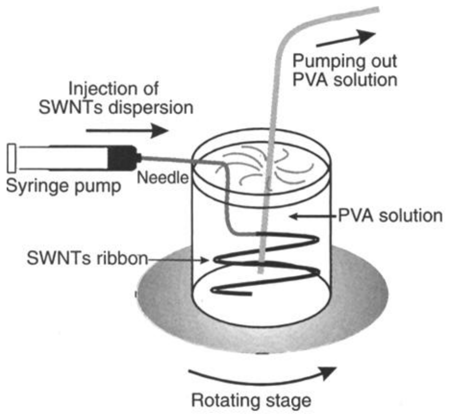

Fig. 2. Schematic of the experimental setup used to make nanotube ribbons. Flow-induced alignment of the nanotubes took place at the tip of the capillary. The ribbons could be drawn in the third dimension and formed a helical structure when the polymer solution was slowly pumped out from the bottom of the container. The injection rate of the SWNT dispersion was varied from 10 to 100 ml/hour. The polymer solution was in a cylindrical container that rotated at speeds ranging from 30 to 150 rpm. The capillary tip from which the nanotube solution was extruded was located at about 3.5 cm from the rotation axis of the polymer solution. The needle or the capillary tube was oriented so that the SWNT injection was tangential to the circular trajectory of the polymer solution. The velocity of the polymer solution at the tip of the capillary could thus be varied from 6.6 to 33 m/min.

nanotube bundles were, on average, mostly oriented along the main axis of the ribbon.

In order to make systems that are more compact, rinsed ribbons can be suspended in air with two extremities supported on solid substrates. As shown in Fig. 3B, capillary forces caused the water to be expelled, and the ribbon collapsed into a dense fiber with a radius of a few micrometers when dry. On the basis of the same principle, fibers several tens of centimeters long can be directly made by slowly pulling ribbons out of water.

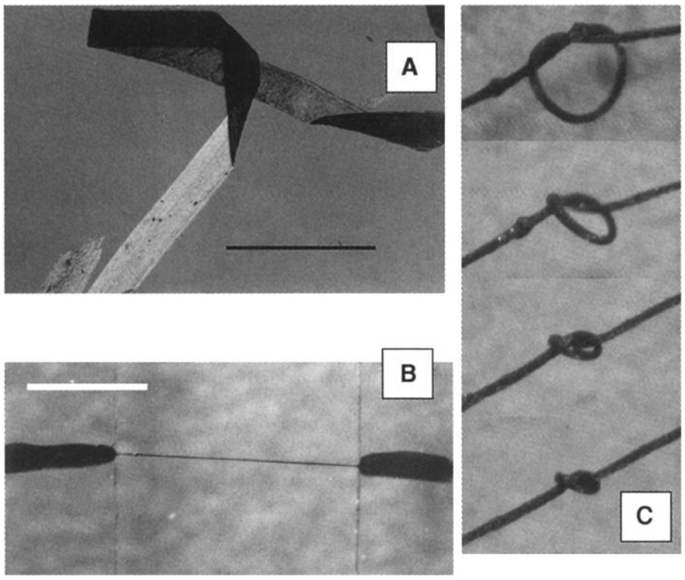

Fig. 3. Optical micrographs of nanotube ribbons and fibers. **(A)** A single folded ribbon between horizontal and vertical crossed polarizers. Vertical or horizontal sections of the ribbon are dark, and the brightest sections are seen when the ribbon makes an angle of 45° with respect to the polarizer axis (scale bar = 1.5 mm). **(B)** A freestanding nanotube fiber between two glass substrates. This fiber was obtained from the collapse and the drying of an initial ribbon, the extremities of which are supported on the glass (scale bar = 1 mm). **(C)** Tying knots reveals the high flexibility and resistance to torsion of the nanotube microfibers. The fiber shown in the pictures has a radius of about 15 μm.

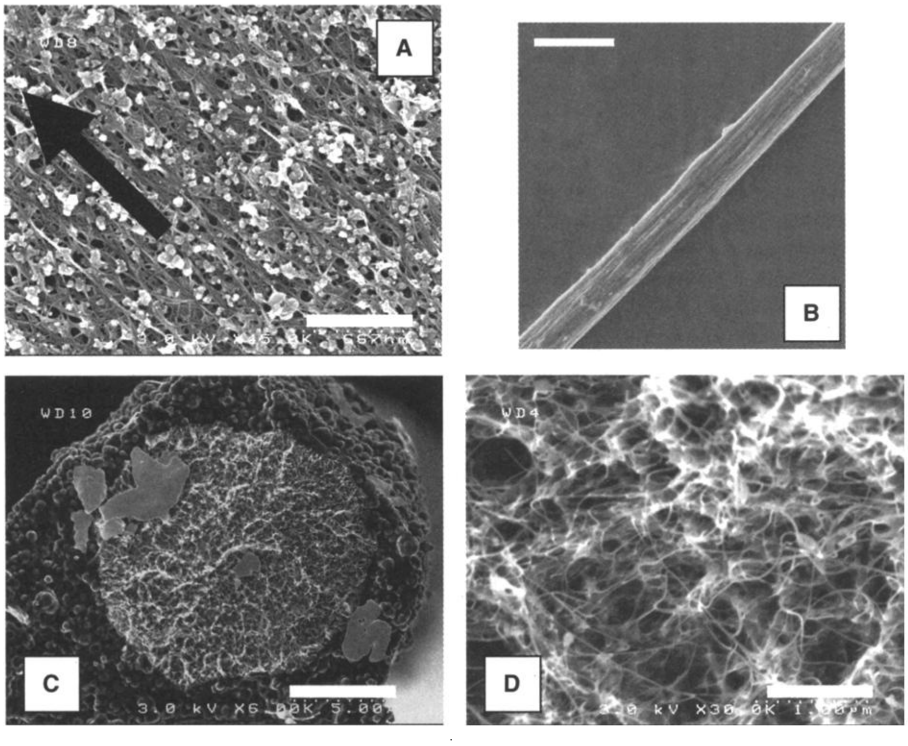

Fig. 4. Scanning electron micrographs at various magnifications. **(A)** A dry ribbon deposited on a glass substrate. The black arrow indicates the main axis of the ribbon, which corresponds to the direction of the initial fluid velocity. Despite the presence of a significant amount of spherical carbon impurities, SWNT bundles are preferentially oriented along the main axis (scale bar = 667 nm). **(B)** A nanotube fiber (scale bar = 25 μm). **(C)** Cross section of a nanotube fiber. The brighter region (more conducting) is mostly composed of SWNTs. It is surrounded by a darker region (less conducting) mostly composed of carbon impurities (scale bar = 16.7 μm). **(D)** Magnification of the bright region in (C) to show the presence of nanotube bundles and the absence of carbon impurities (scale bar = 1 μm).

The diameter of the fibers can be controlled by varying the parameters (injection rate, flow conditions, and dimensions of the capillary tube) that control the initial thickness of the ribbons. By varying these parameters, we made fibers with diameters ranging from a few micrometers to 100 μm. A scanning electron micrograph of a typical fiber is shown in Fig. 4B. Their density was estimated by directly weighing the fibers and calculating their volume from their dimensions. The measurements of several fibers were between 1.3 ± 0.2 and 1.5 ± 0.2 g/cm^3. These results were confirmed by flotation method measurements. This density is about three times greater than the density of classical bucky paper and is two orders of magnitude greater than that of raw material (*10*).

Trying to make knots with SWNT fibers reveals a particularly interesting feature. The fiber does not break as the knot is tightened (Fig. 3C). Hence the fiber can be curved through 360° in a few micrometers. This simple observation demonstrates the flexibility and high resistance to torsion of nanotube fibers as compared to classical carbon fibers. Mechanical measurements show another difference from classical carbon fibers. The SWNT fibers exhibit a plastic behavior at room temperature before they break. This presumably arises from the possible displacement of the nanotubes within the fibers. The slope of the curve strain versus stress decreases when the fiber is under high tensile loading (Fig. 5). In the elastic regime, for smaller deformation, from measurements on several fibers we found that the Young's modulus varied between 9 and 15 GPa. Although far weaker than the modulus of individual nanotubes (*3–5*), the modulus of SWNT fibers is an order of magnitude greater than the modulus of high-quality bucky paper (*12*).

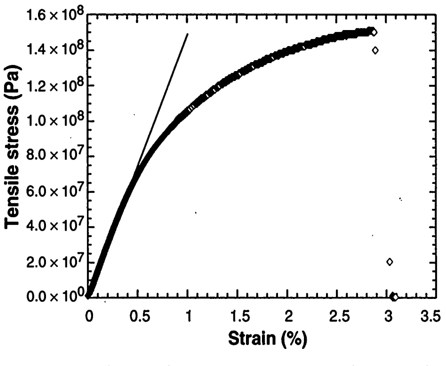

Fig. 5. Mechanical measurements under tensile loading performed at a strain rate of 1% per minute. The modulus deduced at low deformation is about 15 GPa. The fiber exhibits plastic behavior under strong loading.

Finally, an intriguing feature of the present fibers is shown in scanning electron microscopy pictures of the fiber cross section. Two different domains can be distinguished: a well-defined core that mostly contains SWNTs and an external shell that is composed of spherical carbon particles (as evidenced by microprobe analysis) (Fig. 4, C and D). These carbon impurities, which originate directly from the raw material, are randomly distributed in the initial ribbons (Fig. 4A). Hence, the separation within the fibers should take place as the fibers are collapsing under capillary forces and water evaporation from the initial ribbons. This particular feature may open a new route for the large-scale purification of SWNTs. Chemical, irradiative, or thermal removal of the external shell could lead directly to purified SWNTs.

Preliminary four-probe electrical measurements gave a resistivity at room temperature of about 0.1 ohm-cm and a nonmetallic behavior when the temperature was decreased. This value, three orders of magnitude greater than that previously reported for SWNTs (*18–21*), has to be taken with caution because of the presence of the external shell of carbon particles.

Research is currently under way to examine the mechanical and electrical properties of the present ribbons and fibers as the full phase space of nanotube type, purity, concentration, flow, and injection conditions is explored. Further studies are also highly desirable to improve the mechanical properties of SWNT fibers, perhaps through chemical or thermal treatments. More generally, the present method may also be suitable for making fibers out of other kinds of dispersed particles. Although it is intrinsically different from more classical techniques used to make microfibers by pulling or drawing viscoelastic fluids (*22*), it can also be easily scaled up for high-volume production (*23*).

References and Notes

1. G. Overney, W. Zhong, D. Z. Tomanek, *Phys. D* **27**, 93 (1993).
2. D. H. Robertson, D. W. Brenner, J. W. Mintmire, *Phys. Rev. B.* **45**, 12592 (1992).
3. M. M. J. Treacy, T. W. Ebbesen, J. M. Gibson, *Nature* **381**, 678 (1996).
4. J. P. Salvetat *et al.*, *Phys. Rev. Lett.* **85**, 944 (1999).
5. M. R. Falvo *et al.*, *Nature* **389**, 582 (1997).
6. M. S. Dresselhaus, G. Dresselhaus, P. C. Eklund, *Science of Fullerenes and Carbon Nanotubes* (Academic Press, San Diego, CA, 1996).
7. A. Thess *et al.*, *Science* **273**, 483 (1996).
8. C. Journet *et al.*, *Nature* **388**, 756 (1997).
9. J. Chen *et al.*, *Science* **282**, 95 (1998).
10. A. G. Rinzler *et al.*, *Appl. Phys. A* **67**, 29 (1998).
11. An alternative method for making SWNT fibers has recently been published [H. H. Gommans *et al.*, *J. Appl. Phys.* **88**, 2509 (2000)].
12. R. H. Baughman *et al.*, *Science* **284**, 1340 (1999).
13. R. J. Hunter, *Foundations of Colloid Science*, vol. 1 (Oxford Univ. Press, Oxford, 1989).
14. S. Asakura, F. Oosawa, *J. Chem. Phys.* **22**, 1255 (1954).
15. J. M. Bonard *et al.*, *Adv. Mat.* **9**, 827 (1997).
16. M. Doi, S. F. Edwards, *The Theory of Polymer Dynamics* (Oxford Univ. Press, New York, 1986).
17. S. M. Clarke, A. R. Rennie, P. Convert, *Europhys. Lett.* **35**, 233 (1996).
18. H. Dai, E. W. Wong, C. Lieber, *Science* **272**, 523 (1996).
19. J. E. Fisher *et al.*, *Phys. Rev. B* **55**, R4921 (1997).
20. C. L. Kane *et al.*, *Europhys. Lett.* **41**, 683 (1998).
21. J. Hone *et al.*, *Appl. Phys. Lett.* **77**, 666 (2000).
22. I. W. Donald, *J. Mat. Sci.* **22**, 2661 (1987).
23. P. Poulin, B. Vigolo, A. Pénicaud, C. Coulon, CNRS French Patent 0002272 (2000).

24. We gratefully acknowledge R. Baughman for enthusiastic support of this work, R. Canet for assistance in the conductivity measurements, and M. Alrivie for SEM experiments.

20 July 2000; accepted 10 October 2000

Change in the Probability for Earthquakes in Southern California Due to the Landers Magnitude 7.3 Earthquake

Max Wyss[1] and Stefan Wiemer[2]

The Landers earthquake in June 1992 redistributed stress in southern California, shutting off the production of small earthquakes in some regions while increasing the seismicity in neighboring regions, up to the present. This earthquake also changed the ratio of small to large events in favor of more small earthquakes within about 100 kilometers of the epicenter. This implies that the probabilistic estimate for future earthquakes in southern California changed because of the Landers earthquake. The location of the strongest increase in probability for large earthquakes in southern California was the volume that subsequently produced the largest slip in the magnitude 7.1 Hector Mine earthquake of October 1999.

The interdependence of fore-, main-, and aftershocks is self-evident, although the physics of the connecting process is not fully understood. In the months after the event, the 65-km-long rupture of the crust near Landers (*1*) increased the seismicity rate more clearly (*2*) and to larger distances (*3*) than did most mainshocks. The enhanced production of small earthquakes in parts of the volume surrounding the Landers earthquake can be explained by a change in the Coulomb fracture criterion (*4*), which measures the difference between the competing forces that promote and inhibit fracture along preexisting faults (*5*).

We investigated the interdependence between the Landers earthquake and the two largest earthquakes that followed it by 3 hours [near Big Bear with magnitude 6.5 and a rupture length of 20 km (*6*)] and by 7 years [near Hector Mine with magnitude 7.1 and a rupture length of 50 km (*7*)], as well as the sustained decrease and increase of the seismicity rate in neighboring areas of southern California (Fig. 1). In the volumes south of the Hector Mine rupture and north of Big Bear, the production of earthquakes was turned off (dashed lines in Fig. 1) at the time of the Landers earthquake while the production was strongly increased in the volume surrounding the Hector Mine hypocenter and north of Landers (solid lines in Fig. 1). The change of seismicity rates in all four volumes persisted to the end of the data set [1999.7 (decimal year)], which coincides with the time of the Hector Mine earthquake. In three of the examples in Fig. 1, the rate remained approximately constant since the Landers event, whereas it decreased from an exceedingly high to a moderately high level in the Hector Mine volume.

These rate changes are measured by changes in the constant a in the frequency magnitude distribution

$$\log N = a - bM \qquad (1)$$

where N is the number of events with magnitude larger or equal to M. In addition, we examined the change of the ratio of small to large earthquakes, as measured by the b value in Eq. 1, because constants a and b can be used to estimate by extrapolation the recurrence time T of mainshocks with magnitude $M_{\max}$ by

$$T_{\mathrm{L}}(M_{\max}) = \Delta T / 10^{(a - bM_{\max})} \qquad (2)$$

where ΔT is the period over which the N earthquakes have been observed. The abbreviation L stands for "local," meaning the local value for volumes with a constant radius r. The annual local probability P_{L} per unit area A for the occurrence of an earthquake with $M_{\max}$ is the inverse of T_{L}, divided by A

---

[1] Geophysical Institute, University of Alaska, Fairbanks, AK 99775, USA. E-mail: max@giseis.alaska.edu
[2] Federal Institute of Technology, CH-8093, Zürich, Switzerland. E-mail: stefan@seismo.ifg.ethz.ch